https://doi.org/10.5194/egusphere-2025-1117
Preprint. Discussion started: 26 March 2025

Scattering properties and Lidar Characteristics of Asian Dust Particles Based on Realistic Shape Models

Anthony La Luna[1,2], Zhibo Zhang[1,2*], Jianyu Zheng[2,3], Qianqian Song[1], Hongbin Yu[3], Jiachen Ding[4], Ping Yang[4], Masanori Saito[5]

1. Physics Department, University of Maryland Baltimore County (UMBC), Baltimore, MD, USA
2. Goddard Earth Sciences Technology and Research (GESTAR) II, UMBC, Baltimore, MD, USA
3. NASA Goddard Space Flight Center Greenbelt, MD USA
4. Texas A&M University, College Station, TX, USA
5. University of Wyoming, Laramie, WY, USA

Correspondence to: Zhibo Zhang zzbatmos@umbc.edu

https://doi.org/10.5194/egusphere-2025-1117
Preprint. Discussion started: 26 March 2025

Abstract

The lidar backscattering properties of Asian dust particles, namely the lidar ratio (S) and backscattering depolarization ratio (δ), were studied using a discrete dipole approximation (DDA) model. The three-dimensional morphology of the dust particles was reconstructed in fine detail using the focused ion-beam (FIB) tomography technique. An index based on the symmetry of the scattering phase matrix was developed to assess the convergence of random orientation computation using DDA. Both the S and δ exhibit an asymptotic trend with dust particle size: the S initially decreases while the δ increases with size, before both approach their asymptotic values. The lidar properties were found to have statistically insignificant dependence on effective sphericity. The presence of strongly absorbing minerals, such as magnetite, can greatly reduce the dust's single-scattering albedo and δ. Utilizing the robust asymptotic trend behavior, two parameterization schemes were developed: one to estimate the δ of a single dust particle given its size, and the other to estimate the δ of dust particles with a lognormal particle size distribution given the effective radius. The parameterization scheme was compared with results based on the TAMUdust2020 database, showing hexahedrals to reasonably represent realistic geometries with similar physical properties.

https://doi.org/10.5194/egusphere-2025-1117
Preprint. Discussion started: 26 March 2025

1. Introduction

Dust aerosols are an important component of the Earth System, interacting with Earth's energy, water, and carbon cycles. Directly, dust aerosols scatter and absorb both shortwave and longwave radiation, influencing the planet's energy balance (Tegen et al., 1996; Miller and Tegen, 1998; Myhre et al., 2013; Song et al., 2018, 2022). By scattering incoming solar radiation, dust aerosols contribute to cooling the atmosphere and surface regionally, impacting temperatures and affecting atmospheric circulation patterns (Evan et al., 2006; Lau and Kim, 2007; Zhang et al., 2022). For example, Asian dust transportation to the Tibetan Plateau causes direct radiation effects which result in enhancement to the monsoon season (Lau et al., 2006). In addition, the absorption of longwave radiation, particularly thermal infrared radiation, by dust particles leads to surface warming effect by 0.54 W m^{-2} on a global average (Song et al., 2022). Indirectly, dust aerosols serve as nuclei for cloud condensation and ice nucleation, altering cloud microphysical properties and precipitation patterns (Atkinson et al., 2013; Field et al., 2006; Kanji et al., 2017). These indirect effects can further influence regional and global climate dynamics by modifying cloud albedo and distribution (Johnson et al., 2004; Huang et al., 2006; Helmert et al., 2007; Amiri-Farahani et al., 2019).

The transport of this dust also has far-reaching implications. The long-range transport of Asian dust is frequently observed on the United States' west coast with considerable impacts on the air quality and climate (Yu et al., 2012; Creamean et al., 2014; Wu et al., 2015). Moreover, the deposition of dust aerosol during the long-range transport brings essential nutrients such as iron and phosphorus from terrestrial sources to marine ecosystems, facilitating the working of biogeochemical cycles across vast distances (Baker et al., 2003; Yu et al., 2015b; Westberry et

https://doi.org/10.5194/egusphere-2025-1117
Preprint. Discussion started: 26 March 2025

al., 2023). Asian dust deposition in the East China Sea stimulates phytoplankton growth and primary productivity, influencing marine food webs and carbon cycling (Kong, S. S.-K. et al., 2022).

Lidar is an important tool for remote sensing measurements of airborne dust particles. As demonstrated in many previous studies (Omar et al., 2009; Burton et al., 2012), it allows us to distinguish dust aerosols from clouds and other types of aerosols, track their long-range transport and study their evolution as they interact with the environment such as clouds, atmospheric gasses, and other aerosols. Among others, elastic backscattering lidars are one of most widely used types of lidar. For example, Cloud-Aerosol Lidar and Infrared Pathfinder Satellite Observations (CALIPSO), is a NASA-French satellite mission that implements a two-wavelength elastic lidar Cloud-Aerosol Lidar with Orthogonal Polarization (CALIOP) at 532 nm and 1064 nm wavelengths (Winker et al., 2009). Ground-based lidar networks such as the NASA Micro-Pulse Lidar Network (MPLNET) use single wavelength measurements for extinction, backscattering, and depolarization profiles (Welton et al., 2001).

Lidar ratio (S) and depolarization ratio (δ) are two most important parameters for lidar-based remote sensing of aerosols and clouds. For a single dust particle, the S, referred to as the extinction-to-backscatter coefficient, is defined as (Platt, 1979; Ansmann et al., 1992; Mattis et al., 2002; Liu et al., 2002)

$$S = \sigma/\beta = \frac{4\pi}{\omega P_{11}(\theta_s = \pi)}, \qquad (1)$$

https://doi.org/10.5194/egusphere-2025-1117
Preprint. Discussion started: 26 March 2025

where σ is the extinction coefficient and ω and P_{11} are the bulk optical properties of polydisperse dust particles, the single-scattering albedo and phase function of the dust particle, respectively. For the purposes of this paper, P_{11} is normalized to 1 when integrating across all scattering directions. $\beta = P_{11}(\theta_s = \pi)C_{sca}$ is the backscattering coefficient at the exact backscattering direction; defined for a normalized particle size distribution as

$$\beta = \int_{-\infty}^{\infty} P_{11}(r_v, \theta_s = \pi)C_{sca}(r_v)n(r_v)d\ln r_v, \tag{2}$$

Where r_v is the volume-equivalent sphere radius and $n(r_v) = dN/dlnr_v$ defines a normalized particle size distribution ($n(r_v)$). For Raman lidar and high spectral resolution lidar systems, the lidar ratio can be derived directly from the observed extinction and backscatter without assumptions about the composition (Müller et al., 2007). However, for elastic backscattering lidars, the lidar ratio cannot be directly measured. As a result, assumptions need to be made about the composition of the atmosphere. Therefore, it is fundamentally important for elastic lidars like CALIOP and MPLNET to convert the direct attenuated backscatter observations to an extinction profile (Young et al., 2018) and derived quantities such as dust aerosol optical depth (Yu et al., 2015a; Song et al., 2021).

Depolarization ratio δ is the ratio of the perpendicular or cross-polarized component to the parallel component of polarized backscattering signal. For backscattering lidar the depolarization ratio is defined as

$$\delta = \frac{1 - \frac{P_{22}(\theta_s = \pi)}{P_{11}(\theta_s = \pi)}}{1 + \frac{P_{22}(\theta_s = \pi)}{P_{11}(\theta_s = \pi)}}, \tag{3}$$

https://doi.org/10.5194/egusphere-2025-1117
Preprint. Discussion started: 26 March 2025

where P_{ij} is the *ij*-th element of the particle's scattering phase matrix (Kong, S. et al., 2022). δ is highly useful for aerosol and cloud classifications. First of all, if lidar backscattering is dominated by single scattering, δ is close to zero for spherical or quasi-spherical particles like smoke aerosols and water droplets. In contrast, δ is notably greater for nonspherical particles like dust aerosols and ice crystals. Therefore, δ is often used for aerosol type (Kim et al., 2018) and cloud phase classifications (Hu et al., 2009). Moreover, the considerable δ differences between spherical fine particles and nonspherical coarse dust particles also enables the separation of dust extinction from the total extinction profile retrieved by CALIOP (Yu et al., 2015; Song et al., 2021).

Because of the fundamental importance of S and δ for lidar based dust remote sensing, previous studies have made substantial effort to understand the connection between dust particle properties, e.g., shape and size, and their lidar characteristics, in particular the S and δ (e.g., Dubovik et al., 2006; Gasteiger et al., 2011; Liu J. et al., 2015; Kahnert et al., 2020; Saito et al., 2021; Saito and Yang, 2021; Kong, S. et al., 2022). The common methodology used in these studies is to use light scattering models, such as the T-matrix (Mishchenko et al., 1996; Bi and Yang, 2014b) and Discrete Dipole Approximation (DDA) model (Draine and Flatau, 1994, 2013; Yurkin and Hoekstra, 2007, 2011), to compute the scattering properties including S and δ of dust aerosols and then study the potential dependence on particle properties. Although these studies have greatly improved our understanding and paved the foundation for the current aerosol retrieval algorithms, they share a common limitation as they all used hypothetical dust particle shape models, such as spheroid (Dubovik et al., 2006), irregular polyhedron (Saito et al., 2021), Gaussian random sphere (Muinonen et al., 1996; Liu J. et al., 2015; Kahnert et al., 2020), tri-

https://doi.org/10.5194/egusphere-2025-1117
Preprint. Discussion started: 26 March 2025

axial spheroids (Meng et al., 2010; Huang et al., 2023), and super-spheroid (Kong, S. et al., 2022) to simulate dust particle shapes that are weakly or *not* constrained by observations. The reason for this is probably two-fold. Most microscopic observations of dust particles in the literature are two-dimensional (2D) images based on scanning or transmission electron microscopes (SEM or TEM), while three-dimensional (3-D) observations are extremely rare. In addition, the implementation of complex shapes in scattering models is also a challenging task. For example, until recently the widely used T-matrix code based on the extended boundary condition method (Mishchenko et al., 1996) is primarily applicable only to rotationally symmetric particles such as spheroid. It is worth noting that the T-matrix method implementation based on the invariant imbedding T-matrix method is applicable to arbitrary shapes (Bi and Yang, 2014a). Aware of the limitation of hypothetical dust particle shape, these studies often use dust scattering properties from laboratory measurements as benchmark to select an optimal set of hypothetical shapes that are able to generate similar scattering properties, e.g., lidar characteristics, as measurements (Saito et al., 2021; Kong, S. et al., 2022). Nevertheless, the use of hypothetical instead of realistic dust shape inevitably leads to some important questions. Is the match of the dust scattering properties a result of a good shape model or a fortunate coincidence? If an optimal shape model is selected based on one set of dust scattering observations (e.g., δ at 532 nm), can this model automatically simulate other scattering properties (e.g., δ at other wavelengths)? Obviously, one way to address the above questions is to use realistic shape models in the computation of dust scattering properties. A few studies have made attempts along this direction. For example, Lindqvist et al. (2014) developed a so-called stereogrammetric surface retrieval method to construct 3-D dust shapes from 2D SEM dust images. Järvinen et al. (2016) compared the lidar backscattering properties based on the constructed 3-D dust shapes with laboratory

https://doi.org/10.5194/egusphere-2025-1117
Preprint. Discussion started: 26 March 2025

measurements and found reasonable agreements. An important finding from this study is that δ of realistic dust particles at 532 nm first increases with particle size but seems to approach an asymptotic constant value of ~ 0.30 for coarse dust particles.

The main objective of this study is to better understand the lidar backscattering properties of dust particles with realistic shapes. The dust shape models used here are based on the focused ion-beam (FIB) tomography technique, aided by the energy dispersive X-ray spectroscopy (EDX) and SEM imagining, developed by Conny et al. (2014) and Conny and Ortiz-Montalvo (2017), which as far as we know is the most direct and faithful measurement of the shape and morphology of single dust particles. In addition to shape measurement, the EDX is used to measure the mineral composition of dust particles, which in turn enables the estimation of the complex refractive index (CRI) of dust particles. Based on the measured dust particle shape and estimated CRI, Conny et al. (2019, 2020) simulated and studied the scattering properties such as single scattering albedo and phase functions of the dust samples using the DDASCAT model (Draine and Flatau, 1994, 2013).

In this study, we focus on the lidar backscattering properties of realistic dust samples obtained from FIB tomography measurements (Conny et al., 2019). For simplicity, we will refer to these dust samples as "FIB dust samples." We are particularly interested in the following questions: How do the S and δ of realistic dust samples vary with particle size, shape, mineral composition, and lidar spectral channel? The remaining portion of the paper is organized as follows: First, in Section 2, we introduce the dust samples used in this study, along with their origins and properties. We also explain the Amsterdam Discrete Dipole Approximation (ADDA) model and

https://doi.org/10.5194/egusphere-2025-1117
Preprint. Discussion started: 26 March 2025

introduce a convergence index to determine the number of orientations necessary for calculating the optical properties under the random orientation condition. In Section 3, we examine how the lidar backscattering properties of the dust samples depend on dust properties, including size, shape, and mineral composition. In Section 4, we present two dust δ parameterization schemes: one to estimate the δ of a single dust particle based on its size, and the other to estimate the δ of dust particles with a lognormal particle size distribution based on the effective radius. Finally, in Section 5, we summarize the main findings and conclusions of this study.

2. Data and model

2.1. FIB Dust Samples

The fourteen FIB dust particles were obtained from the Mauna Loa Observatory (19° 32′ 10″N, 155° 34′ 34″W) on the island of Hawaii between March 15 and April 26, 2011. Six of these particles were collected during the daytime. Following Conny et al. (2019), these particles will be referred to as the "D" sample (e.g., "3D" indicates that the sample was collected during the daytime of day 3). The other eight particles were collected at night and are referred to as "N" samples. The properties of these particles, including their shape, size, and composition, as well as the measurement techniques, have been extensively documented in (Conny et al., 2019, 2020). Conny et al., (2019) analyzed the back trajectories from the Mauna Loa Observatory during this time interval, suggesting that their samples likely originated as Asian dust. Out of curiosity, we collocated the CALIOP observations with the back trajectories from the Hybrid Single-Particle Lagrangian Integrated Trajectory (HYSPLIT) model (Stein et al., 2015; Rolph et al., 2017) from March 25, 2011, 0000 UTC to March 18, 2011, 0000 UTC, starting from the Mauna Loa Observatory. The lidar depolarization ratio observations and aerosol classification (Figure 1d

https://doi.org/10.5194/egusphere-2025-1117
Preprint. Discussion started: 26 March 2025

and e) results show large amounts of dust along the later portion of the projected path between March 23 and March 24, 2011. The back trajectories and CALIOP observations confirm that the FIB dust samples are likely long-range transported Asian dust particles, consistent with Conny et al. (2019).

https://doi.org/10.5194/egusphere-2025-1117
Preprint. Discussion started: 26 March 2025

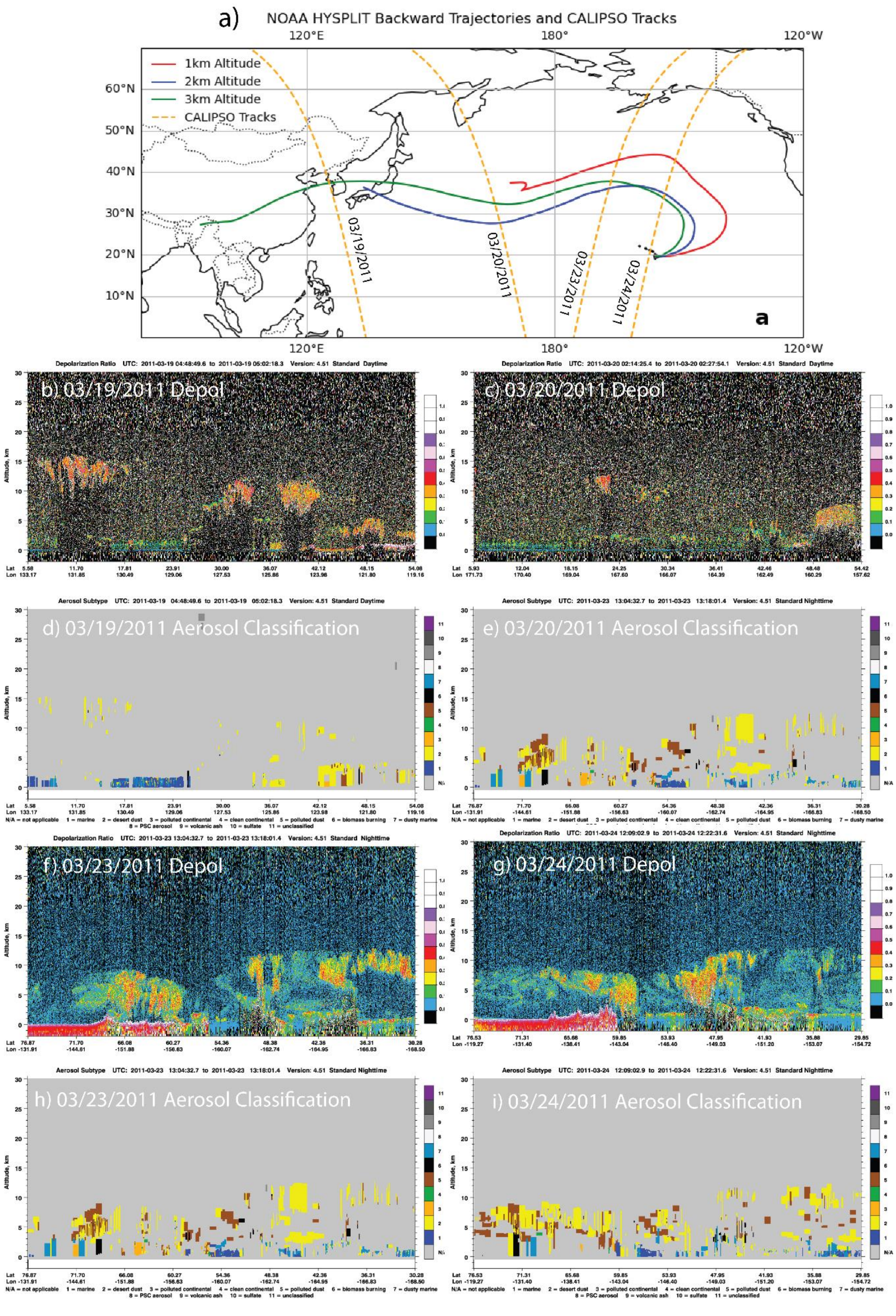

https://doi.org/10.5194/egusphere-2025-1117
Preprint. Discussion started: 26 March 2025

Figure 1. (a) NOAA HYSPLIT Backward Trajectory paths from March 25th, 2011 0000 UTC to March 18th, 2011 0000 UTC starting from Mauna Loa Observatory shown in solid lines. Vertical dashed lines show CALIPSO tracks intersecting with the modeled dust paths. Depolarization ratio and aerosol subtype classification for CALIPSO tracks intersecting with modeled dust paths from NOAA HYSPLIT Backward Trajectory for March 19th, 20th, 23rd, and 24th, 2011 (b-e, respectively). Through δ and aerosol subtype a dust plume was found to be present.

2.2. Dust particle shape and refractive index

As emphasized above, the primary advantage of using FIB dust samples for this study is that the shape and composition of these samples are directly measured. To determine the dust shape, the FIB uses a gallium ion beam, milling through each particle in 15 nm to 20 nm increments. This process results in a stack of 100 to 200 cross-sectional images with dimensions of 1024 by 884 pixels for each particle. These cross-sectional images are then combined to reconstruct highly detailed 3-D dust shapes, composed of three-dimensional pixels or voxels as illustrated by an example in Figure 2.

The collection of dust samples spans a range of sizes. In this study, we quantify this for irregular geometries using the volume equivalent sphere radius. Using this metric, our library covers a range from 0.46 μm to 0.93 μm in volume equivalent radius (r_v). The particle geometries are also assigned two aspect ratios, where orientation is determined through principal component analysis of the voxel coordinates. This analysis aligns the longest axis along the *z*-direction and

https://doi.org/10.5194/egusphere-2025-1117
Preprint. Discussion started: 26 March 2025

the greatest variation from this axis with the *x*- and *y*-directions, aligning with an intuitive understanding of defining aspect ratios in three dimensions. The aspect ratios of these particles vary from 0.629 and 0.398 (particle 2N Ca-S) to more symmetrical particles with aspect ratios of 0.582 and 0.575 (particle 4N1 CaMg).

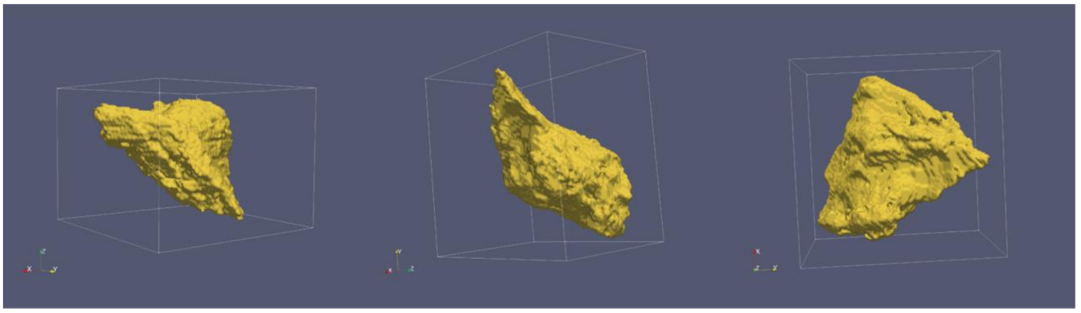

Figure 2. Orthographic projection of a sample dust particle from the FIB reconstructed database, 3D Ca-Rich.

In addition to the FIB-based dust shape reconstruction, Conny et al. (2019) also performed the element composition and mineral phase analysis for the FIB dust samples using the SEM and energy-dispersive X-ray spectroscopy (EDX). They found that the dust samples can be loosely classified into three categories based on the element compositions, the mainly Calcium Magnesium based (Ca-Mg), the Calcium rich (Ca-rich) ones and lastly those primarily composed of Calcium Sulfide (Ca-S). We shall follow their classification and naming convention in this study (see Conny et al., 2019). To determine the refractive index of the dust samples, Conny et al. (2019) first estimated the volume fractions of possible mineral phases in the particles based on the composition analysis results. Then, the complex refractive index of each particle was determined through the average Maxwell-Garnett dielectric function based on the estimated

https://doi.org/10.5194/egusphere-2025-1117
Preprint. Discussion started: 26 March 2025

volume fraction of each mineral phase. It should be noted that the iron-phase composition in the particle was assumed to be either siderite, hematite, or magnetite which has different complex refractive index. Moreover, two sets of complex refractive index were used for each iron-phase mineral to account for the variability induced by optical anisotropy. The combination of mineral differences and refractive index variability lead to several sets of final refractive index after the Maxwell-Garnett average. Take the 3D Ca-Rich particle in Figure 2 for example. Table 1 provides the possible complex refractive index at 589 nm from Conny et al. (2019). Interested readers are referred to their study for more information.

Table 1. The possible complex refractive index at 589 nm of the 3D Ca-Rich particle in Figure 2 from Conny et al. (2019).

Iron-phase mineral	Minimum Refractive Index Real	Minimum Refractive Index Imaginary	Maximum Refractive Index Real	Maximum Refractive Index Imaginary
Magnetite	1.532	2.14E-02	1.660	2.36E-02
Hematite	1.544	2.32E-03	1.681	2.28E-03
Siderite	1.508	1.34E-05	1.648	1.34E-05

In this study, we are interested in the dust scattering properties at three commonly encountered lidar wavelengths, namely, 355 nm, 532 nm, and 1064 nm. For simplicity, we assume the same refractive index from Conny et al. (2019) for all three wavelengths, which is probably reasonable only for the 532 nm. On the other hand, because we assume the refractive index to be invariant with wavelength, the wavelength variation essentially corresponds to the variation of dust

https://doi.org/10.5194/egusphere-2025-1117
Preprint. Discussion started: 26 March 2025

particle size parameter, allowing us to focus on the impact of dust particle size on the lidar scattering properties. The impacts of the spectral variation of refractive index will be investigated in the future studies.

2.3. ADDA model and convergence index of random orientation.

In this study, we utilize the ADDA model to compute the single scattering properties, including the extinction cross section σ_e, single scattering albedo ω, and scattering phase matrix $\boldsymbol{P}$, of each FIB dust particle. The scattering properties of dust particles depend on not only their size, shape, and refractive index, but also their orientations with respect to the incident light. In this study we assume that dust particles are randomly oriented. The theoretical basis and numerical implementation of the ADDA model have been well documented (Yurkin and Hoekstra, 2007, 2011). It has been used in numerous previous studies to compute the scattering properties of aerosol and cloud particles (Yang et al, 2013; Gasteiger, 2011; Collier et al, 2016). The process to generate the inputs from the FIB shape measurements for the discrete dipole approximation (DDA) model has been described in detail in Conny et al. (2019). We use the same inputs and configurations in this study. The only difference is that we use the ADDA model while Conny et al. (2019) used a different DDA model, DDSCAT, by Draine and Flatau (1994). The reason we cannot directly use the DDA simulation results from Conny et al. (2019) is twofold. Firstly, their computations are conducted for an incident light at the 589 nm wavelength, whereas we are interested in lidar wavelengths of 355 nm, 532 nm, and 1064 nm. Secondly, as will be explained later, we will need a greater number of orientations to simulate random orientation for $\boldsymbol{P}$ and lidar backscattering properties (Konoshonkin et al., 2020) than may be sufficient for the σ_e and

https://doi.org/10.5194/egusphere-2025-1117
Preprint. Discussion started: 26 March 2025

ω to converge. In the remainder of this section, we will introduce a practical method to determine if a sufficient number of orientations have been used in the ADDA simulations to ensure convergence in the results for random orientation computations.

For a particle with an irregular shape and arbitrary orientation, the scattering phase matrix ***P*** that relates the incident and scattering Stokes parameters is a 4x4 matrix with 16 elements

$$\begin{bmatrix} P_{11}(\theta_s) & P_{12}(\theta_s) & P_{13}(\theta_s) & P_{14}(\theta_s) \\ P_{21}(\theta_s) & P_{22}(\theta_s) & P_{23}(\theta_s) & P_{24}(\theta_s) \\ P_{31}(\theta_s) & P_{32}(\theta_s) & P_{33}(\theta_s) & P_{34}(\theta_s) \\ P_{41}(\theta_s) & P_{42}(\theta_s) & P_{43}(\theta_s) & P_{44}(\theta_s) \end{bmatrix}, \quad (4)$$

where θ_s is the scattering angle. If the particle is randomly oriented, for any orientation its reciprocal orientation is equally likely. Because of the reciprocal symmetry, the scattering phase matrix for randomly oriented particle with irregular shape reduces to (van de Hulst 1957; Mishchenko et al., 2002; Mishchenko and Yurkin, 2017)

$$\begin{bmatrix} P_{11}(\theta_s) & P_{12}(\theta_s) & P_{13}(\theta_s) & P_{14}(\theta_s) \\ P_{12}(\theta_s) & P_{22}(\theta_s) & P_{23}(\theta_s) & P_{24}(\theta_s) \\ -P_{13}(\theta_s) & -P_{23}(\theta_s) & P_{33}(\theta_s) & P_{34}(\theta_s) \\ P_{14}(\theta_s) & P_{24}(\theta_s) & -P_{34}(\theta_s) & P_{44}(\theta_s) \end{bmatrix}. \quad (5)$$

The symmetry property of the ***P*** matrix for randomly oriented particles in Eq. (5) provides a basis to assess the convergence of random orientation simulations in ADDA. For example, utilizing the fact that $P_{41} = P_{14}$ for randomly oriented particles we can define a convergence index (*CI*) random orientation as

https://doi.org/10.5194/egusphere-2025-1117
Preprint. Discussion started: 26 March 2025

$$CI = \int_0^{\pi} \left(P_{14}(\theta_s) - P_{41}(\theta_s)\right)^2 d\cos(\theta_s). \tag{6}$$

As such, *CI* approaches zero when random orientation computation converges. It should be noted that that *CI* can also be defined based on other symmetric elements of the phase matrix such as $P_{21} = P_{12}$, $P_{31} = -P_{13}$. For practical applications, we usually assume that particles are randomly oriented with an equal number of mirror particles. Under such a condition, or if the particle in question has mirror symmetry itself, the phase matrix has only 6 independent elements in the form (van de Hulst 1957; Mishchenko and Yurkin, 2017; Yang et al., 2023):

$$\begin{bmatrix} P_{11}(\theta_s) & P_{12}(\theta_s) & 0 & 0 \\ P_{12}(\theta_s) & P_{22}(\theta_s) & 0 & 0 \\ 0 & 0 & P_{33}(\theta_s) & P_{34}(\theta_s) \\ 0 & 0 & -P_{34}(\theta_s) & P_{44}(\theta_s) \end{bmatrix}, \tag{7}$$

and a *CI* based on P_{12} or P_{34} must be used.

In the context of ADDA, the orientation of a particle with respect to the incidence is defined using three Euler angles α, β, and γ. To specify a certain orientation, the particle is rotated first α on the *z*-axis, then β on the *y*-axis, and finally γ across the new *z*-axis through the *zyz* convention (Yurkin and Hoekstra, 2020). Then, to produce the scattering properties for a randomly oriented particle, ADDA averages across a large number of orientations. ADDA can do this internally through specified number of evenly spaced intervals across α, β, and γ. For α and β, ADDA calculates the scattering properties for the new orientation while for γ, or the self-rotation angle, it equivalently rotates the scattering plane to improve computational time. It calculates orientations in intervals of $2^n + 1$ for each of α, β, and γ resulting in $(2^n + 1)^3$ total

https://doi.org/10.5194/egusphere-2025-1117
Preprint. Discussion started: 26 March 2025

orientations. To assess if the random orientation convergence has been achieved, one can examine the behavior of *CI* as well as other scattering properties of interest, as a function of the number of orientations. An example using the 3D Ca-Rich dust particle is shown in Figure 3 for $n = 1,2,\ldots,6$. As expected, all properties converge to asymptotic values as n increases from $n = 1$ (i.e., 8 orientations) to $n = 6$ (i.e., 262,144 orientations). On the other hand, it is important to note that the scalar properties such as extinction efficiency and asymmetry factor (Figure 3a), and S and δ (Figure 3b) have converged when $n = 4$, while the *CI* based on certain phase matrix elements (Figure 3c) only converged after $n = 5$. Based on this result, we employ $n = 5$ for the computations in this study. The results in Figure 3 clearly show that although one can assess the convergence of random orientation computation by observing the asymptotic behavior of scalar properties, the *CI* based on phase matrix elements is a more robust index supported by fundamental physics.

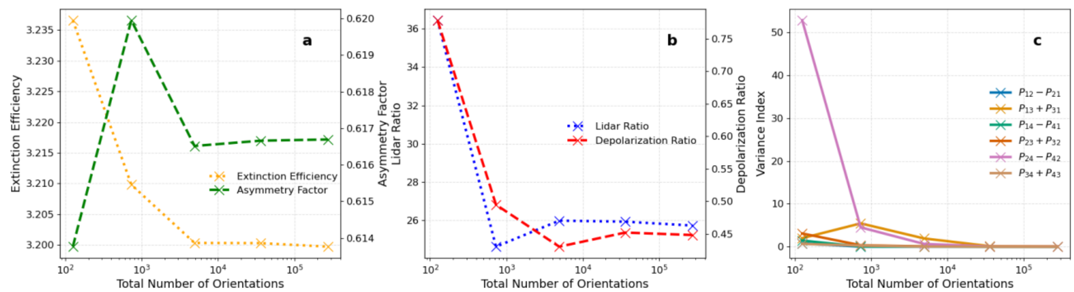

Figure 3. (a) Change in single-scattering albedo and asymmetry factor with increasing orientations for a representation of a randomly oriented particle. (b) The S and depolarization ratio's convergence as the number of orientations used increases. (c) Convergence Index for each of dust particle 3D Ca-Rich's Mueller index pairs at 532 nm. Note figures start at n = 2.

https://doi.org/10.5194/egusphere-2025-1117
Preprint. Discussion started: 26 March 2025

Thus, the error in computations of optical properties through ADDA is strongly tied to the number of orientations used. We find in section 3 constraining refractive index through mineralogy and size through proper characterization of particle size distribution are the largest potential sources of error in these calculations, as ADDA's integration error has been set to less than 10^{-5} and the geometries used are highly detailed, with individual dipole sizes on the order of ~20 nm^3. This makes the numerical error negligible compared to the error in chosen parameters, convergence level, and sample size through the limited set of geometries. The *CI* is a tool to minimize computational error while considering computational cost.

With the help of the newly developed *CI*, we computed the scattering properties of the FIB dust samples for three commonly encountered lidar wavelengths 355 nm, 532 nm, and 1064 nm. For each wavelength, more than 60 ADDA simulations are carried out corresponding to different particles, as well as different refractive indices for each particle as explained above (see section 2.2). Figure 4 shows the phase matrix elements P_{11} and P_{22}/P_{11} for the FIB dust samples for the three lidar wavelengths. Given the realistic morphology and extensive computational methods of determining these optical properties, the FIB dust samples shown in Figure 4 can serve as a benchmark for future studies on mineral dust scattering properties. As one can see in Figure 4 a-c, the values of P_{11} in the forward scattering directions increases systematically from 1064 nm to 532 nm, and 355 nm, which can be explained by the increase of size parameter $x = \pi D/\lambda$ as wavelength decreases. In Figure 4 d-f, the P_{22}/P_{11} shows considerable decreases from 1064 nm to 532 nm, down ~13% on average. In contrast, the changes are relatively small from 532 nm to 355 nm. These features will help us understand the spectral dependence of S and δ shown and discussed in the next section.

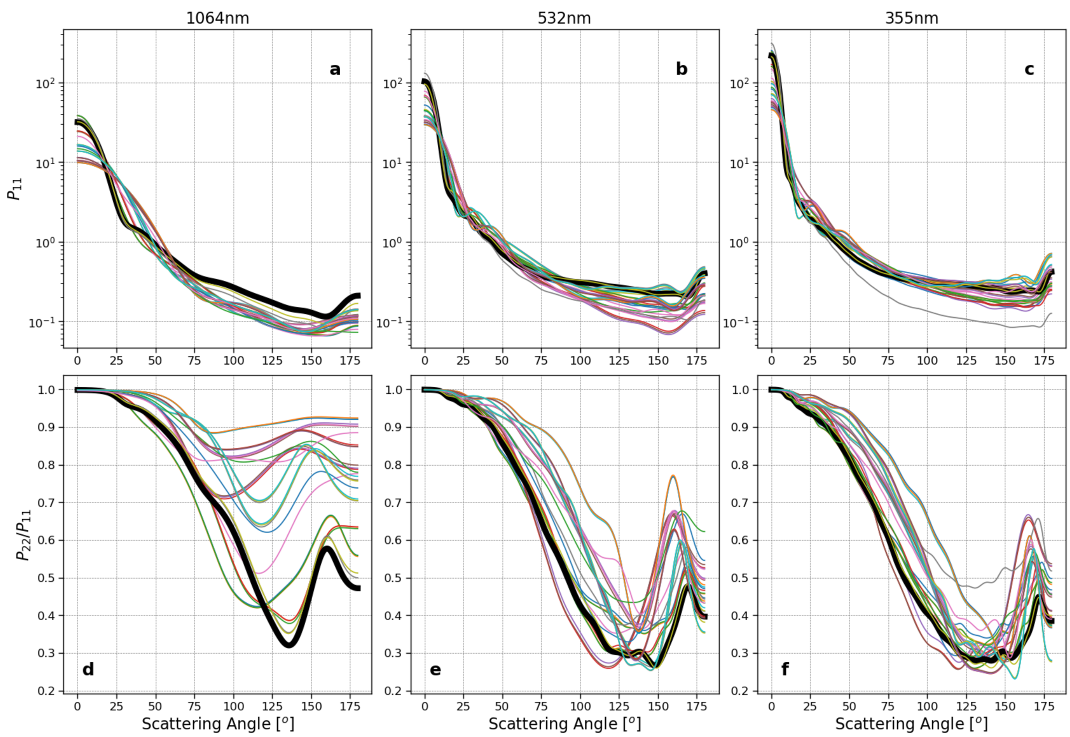

Figure 4. P_{11} and P_{22}/P_{11} for each particle geometry. Results for (a, d) 355 nm, (b, e) 532 nm, (c, f) 1064 nm of each iron-containing mineral phase's minimum refractive index. Highlighted in black is particle 3D Ca-Rich.

3. Sensitivities of lidar ratio and depolarization ratio to particle properties

3.1. Sensitivity to dust particle sizes

In lidar-based aerosol remote sensing, the S - δ diagram is often used to classify aerosols into different types (Burton et al., 2012; Illingworth et al., 2015). The S - δ diagram for the FIB dust samples is shown in Figure 5. Notably, S is negatively correlated with δ when the results for all

https://doi.org/10.5194/egusphere-2025-1117
Preprint. Discussion started: 26 March 2025

three wavelengths are combined (correlation coefficient of 0.83). Specifically, the δ at 1064 nm is smaller than the corresponding values at 532 nm and 355 nm, while the opposite is true for the *S*. The results for 532 nm and 355 nm largely overlap with each other. Recall that the same CRI is used for all three wavelengths, so these spectral differences are caused by the size parameter difference, i.e., the relative size of the particle with respect to the lidar wavelength. To further illustrate this point, we plotted the *S* and δ separately as a function of the dust particle size parameter, shown in Figure 6. Note that the size of the irregular particle can be defined in different ways; here, we adopt the volume-equivalent size.

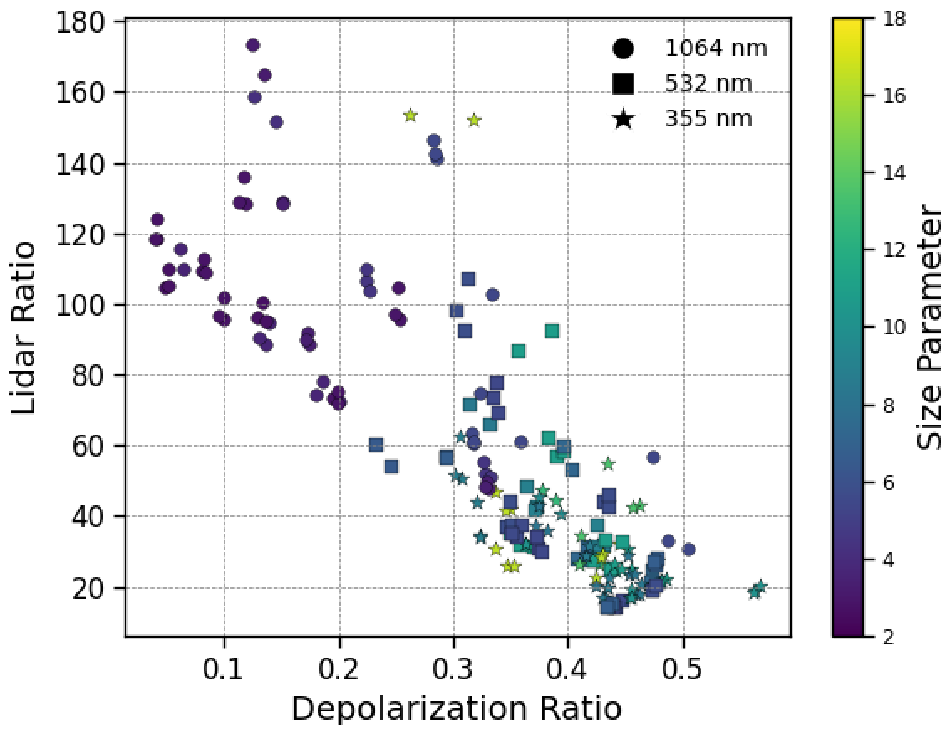

https://doi.org/10.5194/egusphere-2025-1117
Preprint. Discussion started: 26 March 2025

Figure 5. S - δ graph of FIB dust particles at each of 355 nm, 532 nm, and 1064 nm wavelengths for the refractive index of each mineral type found present in the particle.

Figure 6 reveals an interesting asymptotic behavior of lidar properties with respect to size, where S (Figure 6a) and δ (Figure 6b) first decreases and increases, respectively, with size parameters and then seemingly approach their asymptotic values. We use a locally weighted scatterplot smoothing regression (or LOWESS) to fit the trend in lidar optical properties with size parameters. We find that both S and δ plateau around size parameter $x \approx 8$ and then approach to their asymptotic values, $S = 35sr^{-1}$ and $\delta = 0.41$. The asymptotic behavior of lidar properties have also been reported in several previous studies. For example, the S and δ based on the so-called super-spheroid dust model in Kong, S. et al. (2022) showed a similar asymptotic behavior for the size parameter range between 2 and 20 (see their Figure 3), and so is the laboratory measured dust δ in Järvinen et al. (2016) (see their Figure 9).

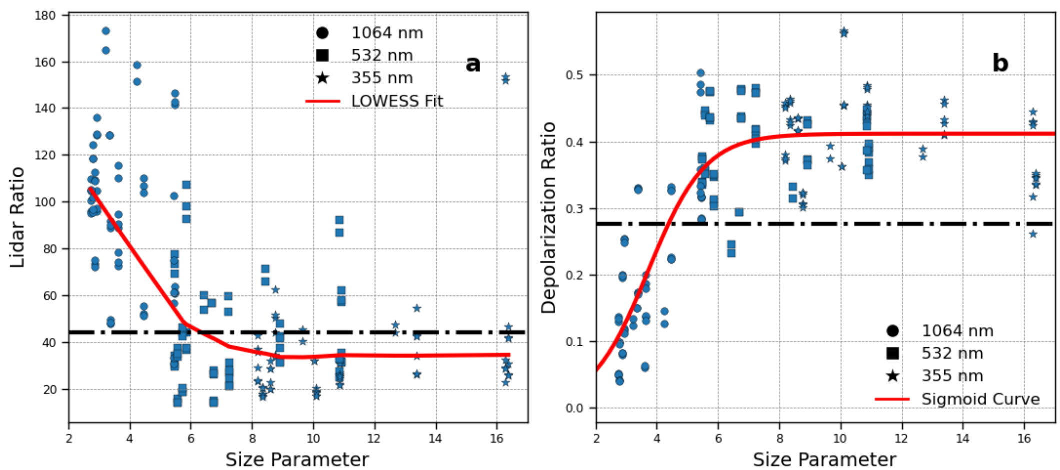

https://doi.org/10.5194/egusphere-2025-1117
Preprint. Discussion started: 26 March 2025

Figure 6. Relationship between dust particle size parameter and (a) S and (b) δ. The red line is a LOWESS fit of the data for S and a Sigmoid function for δ. The black lines correspond to (a) $S = 44\ sr^{-1}$, the S used for CALIPSO's aerosol classification of dust (Kim et al., 2018) and (b) $\delta = 0.277$, the median observed δ of the dust transport region using CALIOP (Liu Z. et al., 2015).

Since S is a function of both $P_{11}(\pi)$ and the ω, we investigate their relative roles in determining the size dependence of S. Figure 7a shows that the values of S lie closely around the $1/P_{11}(\pi)$ line, with the r-square value around 0.97 for a simple regression of $S = 12.9/P_{11}(\pi)$. In contrast, single-scattering albedo ω plays a lesser role in S among the particles tested due to greater similarities in values (Figure 7b). However, the outliers in Figure 7a correspond to points with much lesser ω in Figure 7b, particularly the FIB sample 3D Ca-rich (see Figure 2) using the magnetite refractive index, which has an imaginary refractive index of 0.021 to 0.024, an outlier with a magnitude ten times greater than the other mineral types present (See Table 1). In Figure 7c and d, we plot the variation of $P_{11}(\pi)$ and ω respectively as a function of size parameter. Although the variability of $P_{11}(\pi)$is quite large, especially in the size parameter range between 5 and 10, it generally increases with size parameter. In contrast, the ω in Figure 7b shows a slight decrease with size. These results indicate that $P_{11}(\pi)$ plays a more dominant role than the ω in determining the size dependence of S in these dust samples.

https://doi.org/10.5194/egusphere-2025-1117
Preprint. Discussion started: 26 March 2025

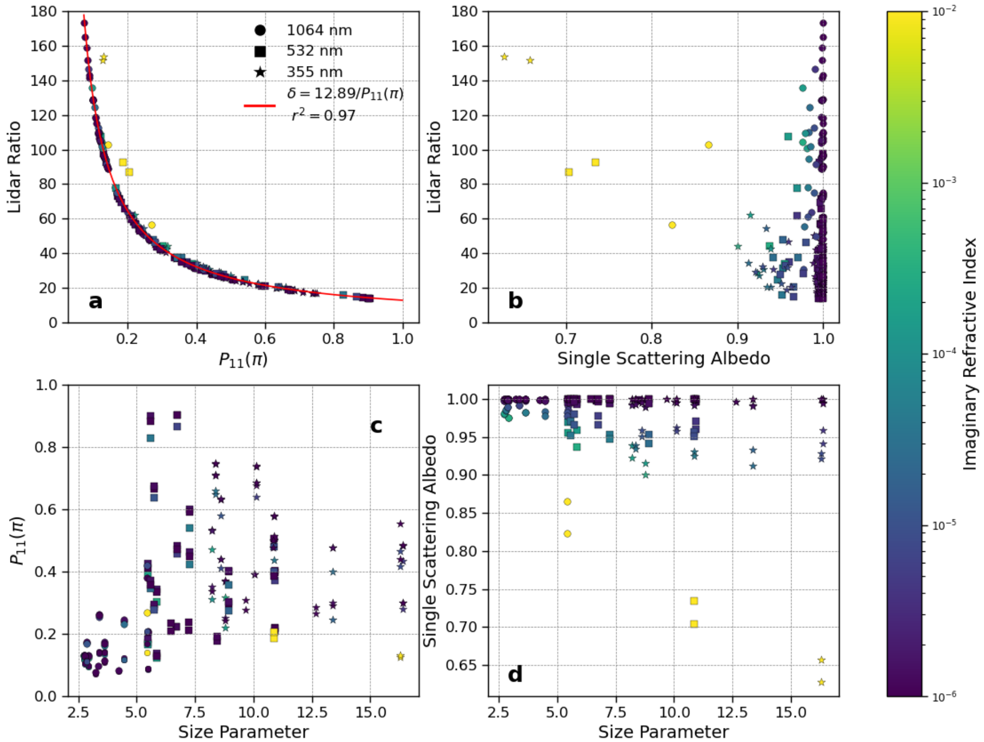

Figure 7. S as a function of a) P_{11} and b) ω. c) P_{11} and d) ω as a function of dust size parameter $x_v = 2\pi r_v/\lambda$. The color of each dot corresponds to the imaginary of the imaginary index.

Following the same thought for the above S analysis, we analyze the role of $P_{11}(\pi)$ and $P_{22}(\pi)$ in determining the asymptotic behavior of δ in Figure 6b. It is seen in Figure 8a and b that both $P_{11}(\pi)$ and $P_{22}(\pi)$ increase with dust size. Interestingly, their ratio $P_{22}(\pi)/P_{11}(\pi)$ first decreases with size and then seems to approach an asymptotic value of 0.4 when dust particles are large. So, the result suggests that the asymptotic trend of δ with respect to dust size is a result of the asymptotic behavior of $P_{22}(\pi)/P_{11}(\pi)$.

https://doi.org/10.5194/egusphere-2025-1117
Preprint. Discussion started: 26 March 2025

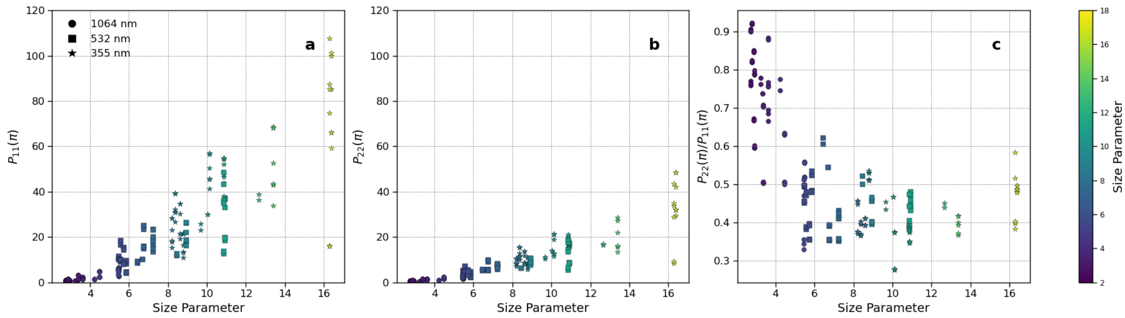

Figure 8. a) $P_{11}(\pi)$, b) $P_{22}(\pi)$ and c) $P_{22}(\pi)/P_{11}(\pi)$ as a function of the dust particle size parameter.

3.2. Sensitivity to dust shape and sphericity

Several studies have shown that constraining particle morphology is important for quantifying the δ of dust particles (Dubovik et al., 2006; Saito et al., 2021; Liu J. et al., 2015; Kahnert et al., 2020; Kong, S. et al., 2022). As explained in the introduction, most of these studies are based on simple hypothetical shape models such as ellipsoid and irregular hexahedrons. In this section, we investigate the dependence of δ on dust sphericity based on the FIB dust samples. As explained in session 2.2, in the baseline simulations each dust sample has different sizes and CRI that corresponds to laboratory measured dust mineralogy. As a result, the differences in δ between different sample particles in the baseline simulations are caused by not only shape but also size and CRI differences. To eliminate the influence of size and CRI and focus on the effect of sphericity, we carried out an additional set of ADDA computations for the 532 nm wavelength, where we used the same CRI of n = 1.5 + 0.005i and the same volume-equivalent radius of 0.5 μm for all the FIB particles but kept the original shape of each particle. The use of the common size and CRI allows us to investigate the dependence of δ on the sphericity index defined as follows (Wadell, 1935; Saito and Yang, 2022):

$$\Psi = \frac{\pi^{1/3}(6V)^{2/3}}{A_s}, \tag{8}$$

Where Ψ is the sphericity, V is the volume of the particle, and A_s is the surface area. By definition, a sphere is Ψ=1, and a perfectly spherical particle has a δ of 0. However, due to the irregularity of the FIB dust sample geometries, their Ψ, more specifically the surface area, is heavily impacted by the level of granularity in the voxel size, similar to the well-known coastline paradox (Steinhaus, 1954). Therefore, we employ the effective sphericity as the average projected area of a particle is not susceptible to the same issues of increasing value with precision (Vouk, 1948; Saito and Yang, 2022):

$$\Psi_{eff} = \frac{\pi^{1/3}(6V)^{2/3}}{4A_{proj}}, \tag{9}$$

Where Ψ_{eff} is the effective sphericity and A_{proj} is the average projected area across all projection directions. This gives us a wide range of effective sphericity between 0.49-0.89. As shown in Figure 9, we find no clear relationship between effective sphericity and δ or S (null hypothesis rejected with $p > 0.05$ for both S and δ). This may be a result of a limited set of geometries of the FIB dust samples. It could also be due to the limitation of the effective sphericity index in Eq. (9) failing to capture the subtle dependence of δ on dust particle shape. Note that other previous studies have also found weak dependence of δ in particle sphericity (e.g., Kong, S. et al., 2022). Further studies are warranted to better understand the relationship

https://doi.org/10.5194/egusphere-2025-1117
Preprint. Discussion started: 26 March 2025

between the δ and morphology of dust particles. But overall, our results seem to suggest that the impact of particle sphericity on δ and S is less important than particle size.

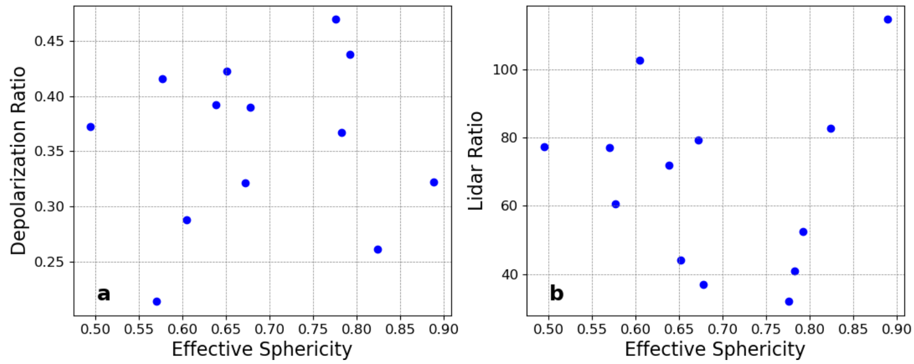

Figure 9. (a) Effective sphericity dependence of δ. (b) Lidar ratio variance with effective sphericity. A common volume is used by constraining the volume equivalent sphere radius to 0.5 μm for each particle as well as a refractive index of $n = 1.5 + .005i$. A wavelength of 532 nm was used.

3.3. Sensitivity to dust mineralogy

Each particle from Conny et al.'s study (2019) was determined to have different amounts of iron in its composition through their EDX spectroscopy tests. Using this data, they determined the refractive index of each particle with the Maxwell-Garnett dielectric function described in section 2.3. The tests resulted in the percentage of elements by mass and volume, but did not reveal the mineral phase within the dust. To account for this, the study uses various possible iron containing mineral phases for each particle to determine the refractive index, as these phases have the greatest variability in possible refractive index for these particles. They also account for birefringence through a minimum and maximum value for refractive index. Each particle was

https://doi.org/10.5194/egusphere-2025-1117
Preprint. Discussion started: 26 March 2025

given a hematite phase, while some had magnetite, ankerite, and/or siderite present. Interested readers are directed to Conny et al. 2019 for further details.

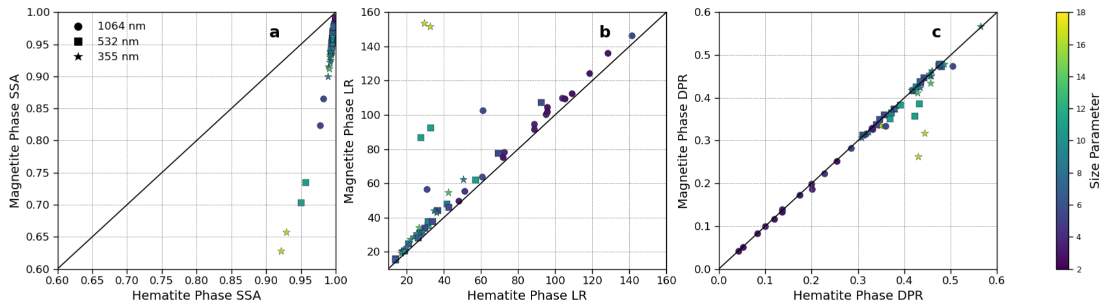

Figure 10. Variation of a) ω, b) *S*, and c) δ for each particle with its magnetite phase and corresponding hematite phase.

Each of these mineral phases has a different CRI, with magnetite being the most absorbing of the iron-containing phases present (see Table 1). This results in considerable variations (up to 32%) in single scattering albedo (Figure 10a), particularly for 3D Ca-Rich particles, which have the highest iron content by mass, ranging from 11.4 % to 7.90 %. In contrast, the next most iron-dense particle (4N1 Ca-Mg) contains only 4.35 % to 1.56 %. Accompanying the reduction in single scattering albedo, the *S* becomes systematically larger (Figure 10b), and the δ becomes smaller (Figure 10c) when hematite is replaced by magnetite. These results underscore the critical role of dust mineralogy in influencing the SSA of dust particles, as highlighted in previous studies (Li et al., 2021; Song et al., 2022, 2024). However, the effects on lidar-derived δ and *S* are comparatively smaller than the impacts on SSA and dust particle size. An important caveat to keep in mind when interpreting these results is that the same dust CRI has been used for all three wavelengths, as mentioned earlier. Dust absorption typically increases with decreasing wavelength in the visible to ultraviolet spectral region, which is not accounted for in our computations. Therefore, the impacts of mineralogy on lidar properties at the 355 nm

https://doi.org/10.5194/egusphere-2025-1117
Preprint. Discussion started: 26 March 2025

wavelength, where dust can have strong absorption, may be underestimated. We will leave this for future studies because the spectral dependence of dust CRI is still highly uncertain due to the lack of reliable observations.

4. Parameterization schemes for dust δ

The results in Section 3 indicate that particle size plays a dominant role in determining the dust δ of FIB dust particles. As shown in Section 3.1, the dust δ exhibits an asymptotic trend with increasing size (see Figure 6b), a pattern also noted in several previous studies (Kong, S. et al., 2022; Järvinen et al., 2016; Kemppinen et al., 2015 a, b). The robustness of this asymptotic trend inspired us to develop two parameterization schemes for δ as a function of dust size, which will be introduced in this section. One scheme is designed for single particles, while the other is intended for ensembles of particles with a particle size distribution. We hope that these parameterization schemes can be used to efficiently estimate the δ of dust particles without resorting to time-consuming scattering simulations.

The parameterization for single particles is straightforward. To model the asymptotic trend of individual particle δ with dust particle size, we employed a sigmoid function as follows:

$$\delta(x) = \frac{\delta_\infty}{1+e^{-a(x+b)}} = \frac{0.41}{1+e^{-1.09(x-3.7)}}, \tag{10}$$

Where $x = \pi r_v/\lambda$ is the particle size parameter. The sigmoid function has three parameters: δ_∞ is the asymptotic value of δ when the size parameter is large. The other two parameters a and b control the shape of the sigmoid function. After a nonlinear curve fitting, we find $\delta_\infty = 0.41$,

https://doi.org/10.5194/egusphere-2025-1117
Preprint. Discussion started: 26 March 2025

$a = 1.09$ and $b = -3.7$ ($R^2 = 0.72$). This simple parameterization can be used to estimate the δ of a single dust particle given its size and the wavelength of interest.

Next, we will use Eq. (10) to construct a parameterization scheme for the volumetric depolarization ratio, ⟨δ⟩ of a dust plume following the widely used lognormal particle size distribution ($n(r_v)$) giving us a value for δ for the ensemble of particles. To this end, we need to first make an approximation. For a given dust particle size distribution $n(r_v) = dN/d\ln r_v$, the rigorous definition of the volumetric δ is given by

$$\langle\delta\rangle = \frac{1-\langle P_{22}\rangle/\langle P_{11}\rangle}{1+\langle P_{22}\rangle/\langle P_{11}\rangle}, \tag{11}$$

where $\langle P_{11}\rangle$ and $\langle P_{22}\rangle$ are the bulk scattering phase matrix elements after the averaging over $n(r_v)$. For example,

$$\langle P_{11}\rangle = \frac{\int_{-\infty}^{\infty} P_{11}(r_v)C_{sca}(r_v)n(r_v)d\ln r_v}{\int_{-\infty}^{\infty} C_{sca}(r_v)n(r_v)d\ln r_v}, \tag{12}$$

where C_{sca} is the scattering cross section of dust particle with the size of r_v. We found that it is difficult to use Eq. (11) to estimate ⟨δ⟩, because neither $\langle P_{11}\rangle$ nor $\langle P_{22}\rangle$ can be easily parameterized with size parameter. To avoid this difficulty, we propose the following approximate way to estimate the $\langle\delta\rangle$ as

$$\langle\delta\rangle \approx \frac{\int_{-\infty}^{\infty} \delta(r_v)C_{\mathrm{sca}}(r_v)n(r_v)\ d\ln r_v}{\int_{-\infty}^{\infty} C_{\mathrm{sca}}(r_v)n(r_v)\ d\ln r_v}, \tag{13}$$

where r_{vg} is the volume median radius, which allows us to use the simple parameterization in Eq. (10). The accuracy of this approximation will be evaluated momentarily. Here, we convert

https://doi.org/10.5194/egusphere-2025-1117
Preprint. Discussion started: 26 March 2025

from size parameter to volume median radius through $x_{vg} = 2\pi r_{vg}/\lambda$ as δ will vary with wavelength. Next, we need to specify the $C_{sca}(r_v)$ of single particles. Unfortunately, the size parameter span of the FIB dust samples is too small to cover the whole dust $n(r_v)$. To solve this problem, we use the TAUMdust2020 database to estimate $C_{sca}(r_v)$. The TAMUdust2020 is a comprehensive database by Saito et al. (2021) that covers the scattering properties of 20 irregular hexahedral shape models over the entire practical range of particle sizes, wavelengths, and CRI of mineral dust particles. Based on the regional dust models recommended by Saito et al. (2021), an ensemble-weighted degree of sphericity of 0.7 is elected to represent the dust particles. For the dust CRI, we use the data from Song et al. (2022) to interpolate the TAMUdust2020 to obtain the $C_{sca}(r_v)$. In Song et al. (2022), three sets of dust CRI corresponding to the low, mean, and high concentration of hematite were used to compute the dust scattering properties and their direct radiative effects. Here we adopt the CRI corresponding to the mean concentration of hematite. Note that the CRI from Song et al. (2022) is spectrally dependent with increasing absorption with decreasing wavelength (see their Figure 2), which means that the 355 nm has the strongest absorption among the three lidar wavelengths considered here. Finally, for the dust $n(r_v)$, we use the lognormal distribution

$$n(r_v) = \frac{dN}{d\ln(r_v)} = \frac{N_0}{\sqrt{2\pi}(\sigma_g)} \exp\left[-\frac{\ln^2(r_v/r_{vg})}{(\sigma_g)^2}\right], \tag{14}$$

Where N_0 is a constant and we use a fixed standard deviation of $\sigma_g = 0.529$, the same standard deviation of the fine mode dust from AERONET's $n(r_v)$ for Cape Verde from Dubovik et al. (2002) used later in Figure 12.

https://doi.org/10.5194/egusphere-2025-1117
Preprint. Discussion started: 26 March 2025

Using the combination of the $\delta(x)$ parameterization in Eq. (10), the $C_{sca}(r_v)$ from the TAMUdust2020 database and the lognormal $n(r_v)$ in Eq. (14), we computed the volumetric dust depolarization ratio $\langle\delta\rangle$ based on the proposed approximation in Eq. (13). The result for the 532 nm $\langle\delta\rangle$ as a function of the effective size parameter is shown in Figure 11a. It is not surprising to see that the volumetric dust δ $\langle\delta(x_{vg})\rangle$ resembles the $\delta(x)$ for the single particles in terms of its size dependence. Further simplification is possible through a fitting of the newly bulk averaged depolarization ratio. We find the depolarization of the FIB realistic particles are well approximated by the following hyperbolic tangent equation:

$$\langle\delta(x_{vg})\rangle \approx 0.41\tanh(0.14x_{vg} + 0.09), \tag{15}$$

with an r-squared value of 0.79 as shown in Figure 11a. While this function is fitted for a wavelength of 532 nm in particular, we found that the results for the 355 nm and 1064 nm wavelengths are almost identical. This is probably because we used the same $\delta(x)$ parameterization for all three wavelengths, and only different C_{sca} due to the use of spectrally dependent CRI in Song et al. (2022). It turns out that the C_{sca} plays a minimal role in the δ value making Eq. (15) a reasonable approximation for all three lidar wavelengths given an effective particle size parameter, x_{vg}. This is supported by the comparison results shown in Figure 11b. The solid lines correspond to the volumetric $\langle\delta\rangle$ for the three wavelengths predicted based on the parameterization Eq. (13). The dotted line corresponds to the $\langle\delta\rangle$ of irregular hexahedral computed based on the TAMUdust2020 database using the Song et al. (2022) dust CRI. It is important to note that the computation for irregular hexahedral is based on the rigorous definition of δ in Eq. (11) without any approximation. Evidently, the two sets of $\langle\delta\rangle$ agree reasonably well in terms of both spectral and size parameter dependencies. Interestingly, a decreasing trend was

https://doi.org/10.5194/egusphere-2025-1117
Preprint. Discussion started: 26 March 2025

observed for the 355 nm δ based on the irregular hexahedral when r_{vg} is larger than about 2 μm to 3 μm, which is not seen in either our parameterization or hexahedral results for other wavelengths. As mentioned above, in the computation for the irregular hexahedral we used the spectrally dependent CRI that has a higher absorption at 355 nm. Recall the result in Figure 10c that indicates δ to decrease with dust absorption. We believe that this decreasing with size trend of δ for large r_{vg} is a result of stronger absorption at 355 nm, reflected in a decrease in SSA for those particles.

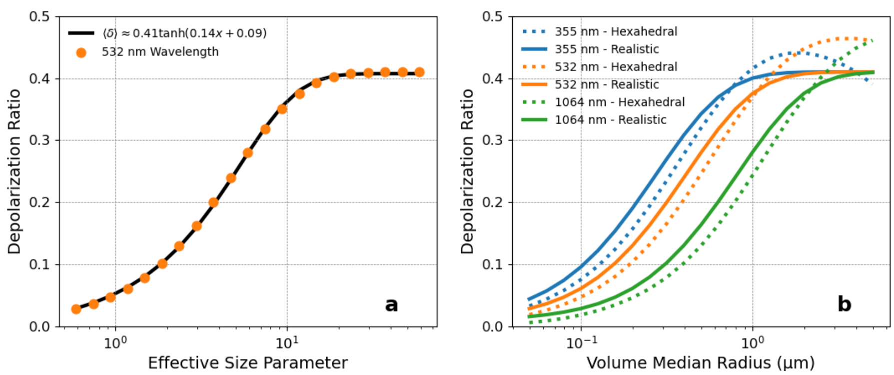

Figure 11: (a) Parameterization of realistic δ for effective size parameter using a hyperbolic tangent function. (b) Depolarization Ratio predicted for a monomodal size distribution with varying volume-equivalent median diameter. The δ for realistic geometries was derived through parameterized approximations, while hexahedral shapes used P_{11} and P_{22} parameters.

The utility of the simple parameterization scheme in Eq. (15) is further demonstrated in terms of simulating the spectral dependence of δ as shown in the following case. Here, we use the climatological dust $n(r_v)$ retrieved by the AERONET at Cape Verde as reported in Dubovik et

https://doi.org/10.5194/egusphere-2025-1117
Preprint. Discussion started: 26 March 2025

al., (2002) (Figure 12a) to compute three sets of volumetric dust $\langle \delta \rangle$ for the three lidar wavelengths using the following three methods:

1. In the first method (black solid lines in Figure 12b), dust scattering properties are based on the irregular hexahedral model from the TAMUdust2020 database. The dust CRI is spectrally dependent from the Song et al. (2022). The $\langle \delta \rangle$ is computed based on the rigorous definition in Eq. (11) with $\langle P_{11} \rangle$ and $\langle P_{22} \rangle$ averaged over $n(r_v)$.
2. In the second method (blue dashed lines in Figure 12b), same as the first method except that the $\langle \delta \rangle$ is computed based on the approximation method in Eq. (13).
3. In the third method (red dotted lines in Figure 12b), the $\langle \delta \rangle$ for each wavelength is simply predicted using the parameterization in Eq. (15) by converting the x_{vg} to r_{vg}.

As such, the comparisons between the three methods enable us to assess the uncertainty associated with each step of approximation. For example, the comparison between method 1 and 2 can help us understand the uncertainty associated with the $\langle \delta \rangle$ computation using the approximation method in Eq. (13). The comparison of method 3 to the other two methods helps us understand the overall accuracy of our simple parameterization.

In order to use the full $n(r_v)$ with method 3, a weighting by backscatter coefficient is utilized such that (Mamouri and Ansmann, 2014)

$$\langle \delta \rangle = \frac{\beta_f \delta_f (1+\delta_c) + \beta_c \delta_c (1+\delta_f)}{\beta_f (1+\delta_c) + \beta_c (1+\delta_f)}, \tag{16}$$

where β is calculated from the TAMUdust2020 database.

https://doi.org/10.5194/egusphere-2025-1117
Preprint. Discussion started: 26 March 2025

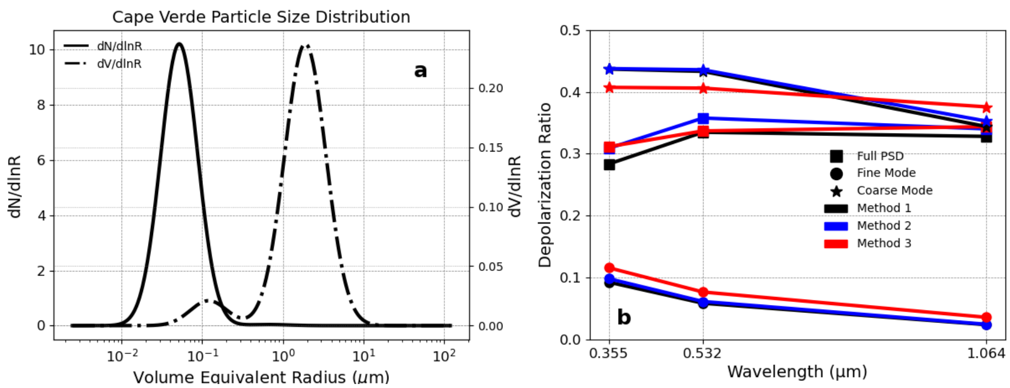

Figure 12. (a) Dust particle size distribution for Cape Verde using AERONET, adapted from Dubovik et al. (2002). Vertical line indicates fine/coarse mode cutoff. (b) Depolarization Ratio of fine and coarse mode for hexahedral dust and FIB reconstruction using approximation methods 1, 2, and 3 as described previously.

The comparisons shown in Figure 12 are promising. First of all, all three methods simulate a substantially smaller δ for the fine mode than the coarse mode. Secondly, the fine mode δ based on all three methods exhibits a decreasing trend with wavelength which is a result of the fast-increasing trend of δ with dust particle size parameter for fine mode dust particles (See Figure 6). The differences in the fine mode δ between the three methods are mostly smaller than 0.05, with the method 3 result based on the simple parameterization scheme slightly larger than the other two methods. Finally, for the coarse mode dust δ, the results based on the simple parameterization (method 3) are close to spectrally neutral and smaller than the other two methods for 355 and 532 nm, while the use of TAMUdust2020 decreases δ at 1064 nm. Interestingly, the full-size distribution δs based on the other two methods exhibit an inverse "v" shape, with the maximum at the 532nm and decreasing toward both 355 nm and 1064 nm. Such an inverse "v" shape spectral signature of dust δ has also been observed recently by (Haarig et

https://doi.org/10.5194/egusphere-2025-1117
Preprint. Discussion started: 26 March 2025

al., 2022) over Leipzig, Germany, in February and March 2021 during a transported Sahara dust event (see their Figure 5). As aforementioned, our δ parameterization scheme does not take into account the spectral dependence of dust CRI and the corresponding change of absorption. In method 2 and 3, we use the CRI from Song et al. (2022) which has a stronger absorption at 355 nm, which leads to a decrease of δ from 532 nm to 355 nm. Therefore, our results indicate that the inverse "v" shape spectral signature of dust δ is a result of competing effects of dust size and absorption. The decrease of δ from 532 nm to 1064 nm is the result of dust size while the decrease from 532 nm to 355 nm is a result of dust absorption. Despite this limitation, the overall accuracy of our parameterization scheme is satisfying, partly due to the error cancellation between the overestimation of the fine mode δ and underestimation of coarse mode δ. For example, after summation of fine and coarse modes, the δ of the whole $n(r_v)$ for the 532nm wavelength is $\langle\delta\rangle \approx 0.335$ based on method 1, while method 3 based on our simple parameterization is $\langle\delta\rangle \approx 0.334$.

Comparing the dust δ of the full $n(r_v)$ to that of fine mode δ and coarse mode δ also gives us interesting results. Both fine and coarse modes individually decrease with wavelength despite the inverse "v" shape spectral signature of the full $n(r_v)$. This characteristic is quite nicely explained by an interpretation of Eq. (16). Across each wavelength, $\beta_f < \beta_c$ so $\langle\delta\rangle$ is greater than a simple average of both fine and coarse modes. But β_c increases with wavelength. Therefore, despite δ_f and δ_c decreasing spectrally, δ_c has a greater weighting in the equation. In other words, more of the backscattered signal is due to larger particles as wavelength increases, which are the particles exhibiting greater depolarization. The competing factors of β and δ further reinforces the absorption and size impact on δ.

https://doi.org/10.5194/egusphere-2025-1117
Preprint. Discussion started: 26 March 2025

The utility of this parameterization likely comes from the inverse problem. Given the reliance on TAMUdust2020 for β, reconstructing the δ from a $n(r_v)$ still requires use of theoretical libraries for some amount of calculation. However, given a retrieved backscattering coefficient, δ, and $n(r_v)$, using Eq. (15) and (16) creates a succinct method of retrieving β_f and β_c, separating fine and coarse fraction of dust according to Mamouri and Ansmann (2014).

Specifically in coarse mode analysis, there are some limitations of our study. The sigmoid parameterization leads to a very flat parameterization of δ for particles greater than 1 μm in volume equivalent radius seen in both Figure 11b and 12b which may be further refined with larger particles, currently unavailable due to computational cost. It is also important to note our study uses a wavelength-independent refractive index based on 589 nm, causing this work to miss some spectral dependency that may cause the coarse mode differences in each wavelength when using the globally averaged refractive index (see Figure 11b). The competing effects of size and mineral composition of dust particles has been observed in studies of spectral dependence of δ (Haarig et al., 2022), which we will investigate in future studies.

5. Conclusions and summary

In this study, we utilized the ADDA model to compute the scattering properties of FIB dust samples and derived the S and δ at three widely used lidar wavelengths: 355 nm, 532 nm, and 1064 nm. The advantage of this study compared to previous work is the use of realistic dust shapes reconstructed through the FIB tomography technique. The characterization of single

https://doi.org/10.5194/egusphere-2025-1117
Preprint. Discussion started: 26 March 2025

scattering properties of these realistic samples through rigorous computational techniques should serve well as benchmark data for the dust scattering community. We investigated the dependence of dust S and δ on dust particle size, shape, and mineral composition. The results lead to the following conclusions:

- Both the S and δ exhibit an asymptotic trend with dust particle size: the S initially decreases while the δ increases with size, before both approach their asymptotic values.
- The lidar properties were found to have only a weak dependence on effective sphericity.
- The presence of strongly absorbing minerals, such as magnetite, can greatly reduce the dust's single scattering albedo and δ, especially at 355 nm.

In addition to these scientific findings, the convergence index introduced in Section 2.3 and the δ parameterization schemes described in Section 4 may be useful for future research on light scattering by nonspherical particles and lidar-based remote sensing. The CI can be used to assess the convergence of random orientation computation using the DDA method. The δ parameterization scheme in Eq. (15) can be used to estimate the δ of dust with a lognormal $n(r_v)$, which can help us understand the variation of dust size based on δ observations and the separation of fine and coarse model dust (Mamouri and Ansmann, 2014).

Author Contributions. ZZ proposed and conceptualized the work, providing both funding acquisition and supervision of the project. All authors contributed to review & editing of the manuscript. JD helped to design the convergence index. MS and PY provided the TAMUdust2020 database for comparison to the FIB dust particles and MS provided insight into particle sphericity. JZ and QS assisted in data curation and interpretation for FIB dust lidar property results and global refractive index data. ASL and ZZ contributed to the original draft

https://doi.org/10.5194/egusphere-2025-1117
Preprint. Discussion started: 26 March 2025

preparation of the manuscript. ASL contributed to the methodology, data collection, interpretation and analysis and data visualization under ZZ supervision and project administration.

https://doi.org/10.5194/egusphere-2025-1117
Preprint. Discussion started: 26 March 2025

References

Amiri-Farahani, A., Allen, R. J., Li, K.-F., & Chu, J.-E. (2019). The Semidirect Effect of Combined Dust and Sea Salt Aerosols in a Multimodel Analysis. *Geophysical Research Letters*, *46*(17–18), 10512–10521. https://doi.org/10.1029/2019GL084590

Ansmann, A., Wandinger, U., Riebesell, M., Weitkamp, C., & Michaelis, W. (1992). Independent measurement of extinction and backscatter profiles in cirrus clouds by using a combined Raman elastic-backscatter lidar. *Applied Optics*, *31*(33), 7113. https://doi.org/10.1364/ao.31.007113

Atkinson, J. D., Murray, B. J., Woodhouse, M. T., Whale, T. F., Baustian, K. J., Carslaw, K. S., et al. (2013). The importance of feldspar for ice nucleation by mineral dust in mixed-phase clouds. *Nature*, *498*(7454), 355–358. https://doi.org/10.1038/nature12278

Baker, A. R., Kelly, S. D., Biswas, K. F., Witt, M., & Jickells, T. D. (2003). Atmospheric deposition of nutrients to the Atlantic Ocean. *Geophysical Research Letters*, *30*(24). https://doi.org/10.1029/2003gl018518

Bi, L., & Yang, P. (2014a). Accurate simulation of the optical properties of atmospheric ice crystals with the invariant imbedding T-matrix method. *Journal of Quantitative Spectroscopy and Radiative Transfer*, *138*, 17–35. https://doi.org/10.1016/j.jqsrt.2014.01.013

Bi, L., & Yang, P. (2014b). High-frequency extinction efficiencies of spheroids: rigorous T-matrix solutions and semi-empirical approximations. *Optics Express*, *22*(9), 10270. https://doi.org/10.1364/oe.22.010270

Bohren, C. F., & Huffman, D. R. (2008). *Absorption and Scattering of Light by Small Particles*. John Wiley & Sons.

Burton, S. P., Ferrare, R. A., Hostetler, C. A., Hair, J. W., Rogers, R. R., Obland, M. D., et al. (2012a). Aerosol classification using airborne High Spectral Resolution Lidar measurements – methodology and examples. *Atmospheric Measurement Techniques*, *5*(1), 73–98. https://doi.org/10.5194/amt-5-73-2012

Burton, S. P., Ferrare, R. A., Hostetler, C. A., Hair, J. W., Rogers, R. R., Obland, M. D., et al. (2012b). AMT - Aerosol classification using airborne High Spectral Resolution Lidar measurements – methodology and examples. *Atmospheric Measurement Techniques*, *5*(1), 73–98. https://doi.org/10.5194/amt-5-73-2012

https://doi.org/10.5194/egusphere-2025-1117
Preprint. Discussion started: 26 March 2025

Conny, J. M., & Ortiz-Montalvo, D. L. (2017). Effect of heterogeneity and shape on optical properties of urban dust based on three-dimensional modeling of individual particles. *Journal of Geophysical Research: Atmospheres*, *122*(18), 9816–9842. https://doi.org/10.1002/2017jd026488

Conny, J. M., Collins, S. M., & Herzing, A. A. (2014). Qualitative Multiplatform Microanalysis of Individual Heterogeneous Atmospheric Particles from High-Volume Air Samples. *Analytical Chemistry*, *86*(19), 9709–9716. https://doi.org/10.1021/ac5022612

Conny, J. M., Willis, R. D., & Ortiz-Montalvo, D. L. (2019). Analysis and Optical Modeling of Individual Heterogeneous Asian Dust Particles Collected at Mauna Loa Observatory. *Journal of Geophysical Research: Atmospheres*, *124*(5), 2702–2723. https://doi.org/10.1029/2018jd029387

Conny, J. M., Willis, R. D., & Ortiz-Montalvo, D. L. (2020). Optical Modeling of Single Asian Dust and Marine Air Particles: A Comparison with Geometric Particle Shapes for Remote Sensing. *Journal of Quantitative Spectroscopy and Radiative Transfer*, *254*(107197). https://doi.org/10.1016/j.jqsrt.2020.107197

Creamean, J. M., Spackman, J. R., Davis, S. M., & White, A. B. (2014). Climatology of long-range transported Asian dust along the West Coast of the United States. *Journal of Geophysical Research: Atmospheres*, *119*(21). https://doi.org/10.1002/2014jd021694

Draine, B. T., & Flatau, P. J. (2013). User Guide for the Discrete Dipole Approximation Code DDSCAT 7.3. *arXiv.Org*. Retrieved from https://arxiv.org/abs/1305.6497

Draine, Bruce T., & Flatau, P. J. (1994). Discrete-Dipole Approximation For Scattering Calculations. *Journal of the Optical Society of America A*, *11*(4), 1491. https://doi.org/10.1364/josaa.11.001491

Dubovik, O., Holben, B., Eck, T. F., Smirnov, A., Kaufman, Y. J., King, M. D., et al. (2002). Variability of Absorption and Optical Properties of Key Aerosol Types Observed in Worldwide Locations. *Journal of the Atmospheric Sciences*, *59*(3), 590–608. https://doi.org/10.1175/1520-0469(2002)059<0590:voaaop>2.0.co;2

Dubovik, O., Sinyuk, A., Lapyonok, T., Holben, B. N., Mishchenko, M., Yang, P., et al. (2006). Application of spheroid models to account for aerosol particle nonsphericity in remote sensing of desert dust. *Journal of Geophysical Research: Atmospheres*, *111*(D11). https://doi.org/10.1029/2005jd006619

https://doi.org/10.5194/egusphere-2025-1117
Preprint. Discussion started: 26 March 2025

Evan, A. T., Dunion, J., Foley, J. A., Heidinger, A. K., & Velden, C. S. (2006). New evidence for a relationship between Atlantic tropical cyclone activity and African dust outbreaks. *Geophysical Research Letters*, *33*(19). https://doi.org/10.1029/2006GL026408

Field, P. R., Möhler, O., Connolly, P., Krämer, M., Cotton, R., Heymsfield, A. J., et al. (2006). Some ice nucleation characteristics of Asian and Saharan desert dust. *Atmospheric Chemistry and Physics*, *6*(10), 2991–3006. https://doi.org/10.5194/acp-6-2991-2006

Gasteiger, J., Wiegner, M., Groß, S., Freudenthaler, V., Toledano, C., Tesche, M., & Kandler, K. (2011). Modelling lidar-relevant optical properties of complex mineral dust aerosols. *Tellus B: Chemical and Physical Meteorology*, *63*(4), 725. https://doi.org/10.1111/j.1600-0889.2011.00559.x

Gasteiger, J. K. (2011, December 6). *Retrieval of microphysical properties of desert dust and volcanic ash aerosols from ground-based remote sensing* (Text.PhDThesis). Ludwig-Maximilians-Universität München. Retrieved from https://edoc.ub.uni-muenchen.de/13786/

Goldsmith, J. (2016). *High Spectral Resolution Lidar (HSRL) Instrument Handbook*. Office of Scientific and Technical Information (OSTI). https://doi.org/10.2172/1251392

Haarig, M., Ansmann, A., Engelmann, R., Baars, H., Toledano, C., Torres, B., et al. (2022). First triple-wavelength lidar observations of depolarization and extinction-to-backscatter ratios of Saharan dust. *Atmospheric Chemistry and Physics*, *22*(1), 355–369. https://doi.org/10.5194/acp-22-355-2022

Helmert, J., Heinold, B., Tegen, I., Hellmuth, O., & Wendisch, M. (2007). On the direct and semidirect effects of Saharan dust over Europe: A modeling study. *Journal of Geophysical Research: Atmospheres*, *112*(D13). https://doi.org/10.1029/2006JD007444

Hu, Y., Winker, D., Vaughan, M., Lin, B., Omar, A., Trepte, C., et al. (2009). CALIPSO/CALIOP Cloud Phase Discrimination Algorithm. *Journal of Atmospheric and Oceanic Technology*, *26*(11), 2293–2309. https://doi.org/10.1175/2009jtecha1280.1

Huang, J., Lin, B., Minnis, P., Wang, T., Wang, X., Hu, Y., et al. (2006). Satellite-based assessment of possible dust aerosols semi-direct effect on cloud water path over East Asia. *Geophysical Research Letters*, *33*(19). https://doi.org/10.1029/2006GL026561

Huang, Y., Kok, J. F., Saito, M., & Muñoz, O. (2023). Single-scattering properties of ellipsoidal dust aerosols constrained by measured dust shape distributions. *Atmospheric*

https://doi.org/10.5194/egusphere-2025-1117
Preprint. Discussion started: 26 March 2025

Chemistry and Physics, *23*(4), 2557–2577. https://doi.org/10.5194/acp-23-2557-2023

Hulst, H. C. van de (Hendrik C. (1981). *Light scattering by small particles*. New York : Dover Publications. Retrieved from http://archive.org/details/lightscatteringb0000huls

Illingworth, A. J., Barker, H. W., Beljaars, A., Ceccaldi, M., Chepfer, H., Clerbaux, N., et al. (2015). The EarthCARE Satellite: The Next Step Forward in Global Measurements of Clouds, Aerosols, Precipitation, and Radiation. *Bulletin of the American Meteorological Society*, *96*(8), 1311–1332. https://doi.org/10.1175/bams-d-12-00227.1

Järvinen, E., Kemppinen, O., Nousiainen, T., Kociok, T., Möhler, O., Leisner, T., & Schnaiter, M. (2016). Laboratory investigations of mineral dust near-backscattering depolarization ratios. *Journal of Quantitative Spectroscopy and Radiative Transfer*, *178*, 192–208. https://doi.org/10.1016/j.jqsrt.2016.02.003

Johnson, B. T., Shine, K. P., & Forster, P. M. (2004). The semi-direct aerosol effect: Impact of absorbing aerosols on marine stratocumulus. *Quarterly Journal of the Royal Meteorological Society*, *130*(599), 1407–1422. https://doi.org/10.1256/qj.03.61

Kahnert, M., Kanngießer, F., Järvinen, E., & Schnaiter, M. (2020). Aerosol-optics model for the backscatter depolarisation ratio of mineral dust particles. *Journal of Quantitative Spectroscopy and Radiative Transfer*, *254*(107177). https://doi.org/10.1016/j.jqsrt.2020.107177

Kanji, Z. A., Ladino, L. A., Wex, H., Boose, Y., Burkert-Kohn, M., Cziczo, D. J., & Krämer, M. (2017). Overview of Ice Nucleating Particles. *Meteorological Monographs*, *58*, 1.1-1.33. https://doi.org/10.1175/amsmonographs-d-16-0006.1

Kemppinen, O., Nousiainen, T., & Jeong, G. Y. (2015). Effects of dust particle internal structure on light scattering. *Atmospheric Chemistry and Physics*, *15*(20), 12011–12027. https://doi.org/10.5194/acp-15-12011-2015

Kemppinen, Osku, Nousiainen, T., & Lindqvist, H. (2015). The impact of surface roughness on scattering by realistically shaped wavelength-scale dust particles. *Journal of Quantitative Spectroscopy and Radiative Transfer*, *150*, 55–67. https://doi.org/10.1016/j.jqsrt.2014.05.024

Kim, M.-H., Omar, A. H., Tackett, J. L., Vaughan, M. A., Winker, D. M., Trepte, C. R., et al. (2018). The CALIPSO version 4 automated aerosol classification and lidar ratio selection algorithm. *Atmospheric Measurement Techniques*, *11*(11), 6107–6135.

https://doi.org/10.5194/egusphere-2025-1117
Preprint. Discussion started: 26 March 2025

https://doi.org/10.5194/amt-11-6107-2018

Kong, S., Sato, K., & Bi, L. (2022). Lidar Ratio–Depolarization Ratio Relations of Atmospheric Dust Aerosols: The Super-Spheroid Model and High Spectral Resolution Lidar Observations. *Journal of Geophysical Research: Atmospheres*, *127*(4). https://doi.org/10.1029/2021jd035629

Kong, S. S.-K., Pani, S. K., Griffith, S. M., Ou-Yang, C.-F., Babu, S. R., Chuang, M.-T., et al. (2022). Distinct transport mechanisms of East Asian dust and the impact on downwind marine and atmospheric environments. *Science of The Total Environment*, *827*, 154255. https://doi.org/10.1016/j.scitotenv.2022.154255

Konoshonkin, A., Kustova, N., Borovoi, A., Tsekeri, A., & Gasteiger, J. (2020). Using the Physical Optics Approximation for Estimating the Light Scattering Properties of Large Dust Particles for Lidar Applications. *EPJ Web of Conferences*, *237*, 08025. https://doi.org/10.1051/epjconf/202023708025

Lau, K. M., & Kim, K. M. (2007). Cooling of the Atlantic by Saharan dust. *Geophysical Research Letters*, *34*(23). https://doi.org/10.1029/2007GL031538

Lau, K. M., Kim, M. K., & Kim, K. M. (2006). Asian summer monsoon anomalies induced by aerosol direct forcing: the role of the Tibetan Plateau. *Climate Dynamics*, *26*(7–8), 855–864. https://doi.org/10.1007/s00382-006-0114-z

Li, L., Mahowald, N. M., Miller, R. L., García-Pando, C. P., Klose, M., Hamilton, D. S., et al. (2021). Quantifying the range of the dust direct radiative effect due to source mineralogy uncertainty. *Atmospheric Chemistry and Physics*, *21*(5), 3973–4005. https://doi.org/10.5194/acp-21-3973-2021

Lindqvist, H., Jokinen, O., Kandler, K., Scheuvens, D., & Nousiainen, T. (2014). Single scattering by realistic, inhomogeneous mineral dust particles with stereogrammetric shapes. *Atmospheric Chemistry and Physics*, *14*(1), 143–157. https://doi.org/10.5194/acp-14-143-2014

Liu, J., Yang, P., & Muinonen, K. (2015). Dust-aerosol optical modeling with Gaussian spheres: Combined invariant-imbedding T-matrix and geometric-optics approach. *Journal of Quantitative Spectroscopy and Radiative Transfer*, *161*, 136–144. https://doi.org/10.1016/j.jqsrt.2015.04.003

Liu, Z., Winker, D., Omar, A., Vaughan, M., Kar, J., Trepte, C., et al. (2015). Evaluation of

https://doi.org/10.5194/egusphere-2025-1117
Preprint. Discussion started: 26 March 2025

CALIOP 532 nm aerosol optical depth over opaque water clouds. *Atmospheric Chemistry and Physics*, *15*(3), 1265–1288. https://doi.org/10.5194/acp-15-1265-2015

Liu, Zhaoyan, Sugimoto, N., & Murayama, T. (2002). Extinction-to-backscatter ratio of Asian dust observed with high-spectral-resolution lidar and Raman lidar. *Applied Optics*, *41*(15), 2760. https://doi.org/10.1364/ao.41.002760

Mamouri, R. E., & Ansmann, A. (2014). Fine and coarse dust separation with polarization lidar. *Atmospheric Measurement Techniques*, *7*(11), 3717–3735. https://doi.org/10.5194/amt-7-3717-2014

Mattis, I., Ansmann, A., Müller, D., Wandinger, U., & Althausen, D. (2002). Dual-wavelength Raman lidar observations of the extinction-to-backscatter ratio of Saharan dust. *Geophysical Research Letters*, *29*(9). https://doi.org/10.1029/2002gl014721

Meng, Z., Yang, P., Kattawar, G. W., Bi, L., Liou, K. N., & Laszlo, I. (2010). Single-scattering properties of tri-axial ellipsoidal mineral dust aerosols: A database for application to radiative transfer calculations. *Journal of Aerosol Science*, *41*(5), 501–512. https://doi.org/10.1016/j.jaerosci.2010.02.008

Miller, R. L., & Tegen, I. (1998). Climate Response to Soil Dust Aerosols. *Journal of Climate*, *11*(12), 3247–3267. https://doi.org/10.1175/1520-0442(1998)011<3247:crtsda>2.0.co;2

Mishchenko, M. I., & Yurkin, M. A. (2017). On the concept of random orientation in far-field electromagnetic scattering by nonspherical particles. *Optics Letters*, *42*(3), 494. https://doi.org/10.1364/ol.42.000494

Mishchenko, M. I., Travis, L. D., & Mackowski, D. W. (1996). T-matrix computations of light scattering by nonspherical particles: A review. *Journal of Quantitative Spectroscopy and Radiative Transfer*, *55*(5), 535–575. https://doi.org/10.1016/0022-4073(96)00002-7

Mishchenko, M. I., Travis, L. D., & Lacis, A. A. (2002). *Scattering, Absorption, and Emission of Light by Small Particles*. Cambridge University Press.

Muinonen, K., Nousiainen, T., Fast, P., Lumme, K., & Peltoniemi, J. I. (1996). Light scattering by Gaussian random particles: Ray optics approximation. *Journal of Quantitative Spectroscopy and Radiative Transfer*, *55*(5), 577–601. https://doi.org/10.1016/0022-4073(96)00003-9

Müller, D., Ansmann, A., Mattis, I., Tesche, M., Wandinger, U., Althausen, D., & Pisani, G. (2007). Aerosol-type-dependent lidar ratios observed with Raman lidar. *Journal of*

https://doi.org/10.5194/egusphere-2025-1117
Preprint. Discussion started: 26 March 2025

Geophysical Research: Atmospheres, *112*(D16). https://doi.org/10.1029/2006jd008292

Myhre, G., Samset, B. H., Schulz, M., Balkanski, Y., Bauer, S., Berntsen, T. K., et al. (2013). Radiative forcing of the direct aerosol effect from AeroCom Phase II simulations. *Atmospheric Chemistry and Physics*, *13*(4), 1853–1877. https://doi.org/10.5194/acp-13-1853-2013

Omar, A. H., Winker, D. M., Vaughan, M. A., Hu, Y., Trepte, C. R., Ferrare, R. A., et al. (2009). The CALIPSO Automated Aerosol Classification and Lidar Ratio Selection Algorithm. *Journal of Atmospheric and Oceanic Technology*, *26*(10), 1994–2014. https://doi.org/10.1175/2009JTECHA1231.1

Platt, C. M. R. (1979). Remote Sounding of High Clouds: I. Calculation of Visible and Infrared Optical Properties from Lidar and Radiometer Measurements. *Journal of Applied Meteorology*, *18*(9), 1130–1143. https://doi.org/10.1175/1520-0450(1979)018<1130:rsohci>2.0.co;2

Rolph, G., Stein, A., & Stunder, B. (2017). Real-time Environmental Applications and Display sYstem: READY. *Environmental Modelling & Software*, *95*, 210–228. https://doi.org/10.1016/j.envsoft.2017.06.025

Saito, M., & Yang, P. (2021). Advanced Bulk Optical Models Linking the Backscattering and Microphysical Properties of Mineral Dust Aerosol. *Geophysical Research Letters*, *48*(17). https://doi.org/10.1029/2021gl095121

Saito, M., & Yang, P. (2022). Generalization of Atmospheric Nonspherical Particle Size: Interconversions of Size Distributions and Optical Equivalence. *Journal of the Atmospheric Sciences*, *79*(12), 3333–3349. https://doi.org/10.1175/jas-d-22-0086.1

Saito, M., Yang, P., Ding, J., & Liu, X. (2021). A comprehensive database of the optical properties of irregular aerosol particles for radiative transfer simulations. *Journal of the Atmospheric Sciences*, *78*(7), 2089–2111. https://doi.org/10.1175/jas-d-20-0338.1

Song, Q., Zhang, Z., Yu, H., Kato, S., Yang, P., Colarco, P., et al. (2018). Net radiative effects of dust in the tropical North Atlantic based on integrated satellite observations and in situ measurements. *Atmospheric Chemistry and Physics*, *18*(15), 11303–11322. https://doi.org/10.5194/acp-18-11303-2018

Song, Q., Zhang, Z., Yu, H., Ginoux, P., & Shen, J. (2021). Global dust optical depth climatology derived from CALIOP and MODIS aerosol retrievals on decadal timescales:

regional and interannual variability. *Atmospheric Chemistry and Physics*, *21*(17), 13369–13395. https://doi.org/10.5194/acp-21-13369-2021

Song, Q., Zhang, Z., Yu, H., Kok, J. F., Di Biagio, C., Albani, S., et al. (2022). Size-resolved dust direct radiative effect efficiency derived from satellite observations. *Atmospheric Chemistry and Physics*, *22*(19), 13115–13135. https://doi.org/10.5194/acp-22-13115-2022

Song, Q., Ginoux, P., Ageitos, M. G., Miller, R. L., Obiso, V., & García-Pando, C. P. (2024). Modeling impacts of dust mineralogy on fast climate response. *Atmospheric Chemistry and Physics*, *24*(12), 7421–7446. https://doi.org/10.5194/acp-24-7421-2024

Stein, A. F., Draxler, R. R., Rolph, G. D., Stunder, B. J. B., Cohen, M. D., & Ngan, F. (2015). NOAA's HYSPLIT Atmospheric Transport and Dispersion Modeling System. *Bulletin of the American Meteorological Society*, *96*(12), 2059–2077. https://doi.org/10.1175/bams-d-14-00110.1

Tegen, I., Lacis, A. A., & Fung, I. (1996). The influence on climate forcing of mineral aerosols from disturbed soils. *Nature*, *380*(6573), 419–422. https://doi.org/10.1038/380419a0

Wadell, H. (1935). Volume, Shape, and Roundness of Quartz Particles. *The Journal of Geology*, *43*(3), 250–280. https://doi.org/10.1086/624298

Welton, E. J., Campbell, J. R., Spinhirne, J. D., & Scott III, V. S. (2001). Global monitoring of clouds and aerosols using a network of micropulse lidar systems. In *SPIE Proceedings*. SPIE. https://doi.org/10.1117/12.417040

Westberry, T. K., Behrenfeld, M. J., Shi, Y. R., Yu, H., Remer, L. A., & Bian, H. (2023). Atmospheric nourishment of global ocean ecosystems. *Science*, *380*(6644). Retrieved from https://www.science.org/doi/full/10.1126/science.abq5252

Winker, D. M., Vaughan, M. A., Omar, A., Hu, Y., Powell, K. A., Liu, Z., et al. (2009). Overview of the CALIPSO Mission and CALIOP Data Processing Algorithms. *Journal of Atmospheric and Oceanic Technology*, *26*(11), 2310–2323. https://doi.org/10.1175/2009jtecha1281.1

Wu, Y., Han, Z., Nazmi, C., Gross, B., & Moshary, F. (2015). A trans-Pacific Asian dust episode and its impacts to air quality in the east coast of U.S. *Atmospheric Environment*, *106*, 358–368. https://doi.org/10.1016/j.atmosenv.2015.02.013

Yang, P., Ding, J., & Kattawar, G. W. (2023). Applications of Maxwell's equations to light scattering by dielectric particles. In *Light, Plasmonics and Particles* (pp. 133–147).

https://doi.org/10.5194/egusphere-2025-1117
Preprint. Discussion started: 26 March 2025

Elsevier. https://doi.org/10.1016/b978-0-323-99901-4.00011-1

Young, S. A., Vaughan, M. A., Garnier, A., Tackett, J. L., Lambeth, J. D., & Powell, K. A. (2018). Extinction and optical depth retrievals for CALIPSO's Version 4 data release. *Atmospheric Measurement Techniques*, *11*(10), 5701–5727. https://doi.org/10.5194/amt-11-5701-2018

Yu, H., Remer, L. A., Chin, M., Bian, H., Tan, Q., Yuan, T., & Zhang, Y. (2012). Aerosols from Overseas Rival Domestic Emissions over North America. *Science*, *337*(6094). Retrieved from https://www.science.org/doi/10.1126/science.1217576

Yu, H., Chin, M., Bian, H., Yuan, T., Prospero, J. M., Omar, A. H., et al. (2015). Quantification of trans-Atlantic dust transport from seven-year (2007–2013) record of CALIPSO lidar measurements. *Remote Sensing of Environment*, *159*, 232–249. https://doi.org/10.1016/j.rse.2014.12.010

Yu, H., Chin, M., Yuan, T., Bian, H., Remer, L. A., Prospero, J. M., et al. (2015). The fertilizing role of African dust in the Amazon rainforest: A first multiyear assessment based on data from Cloud-Aerosol Lidar and Infrared Pathfinder Satellite Observations. *Geophysical Research Letters*, *42*(6), 1984–1991. https://doi.org/10.1002/2015GL063040

Yurkin, M. A., & Hoekstra, A. G. (2020). User manual for the discrete dipole approximation code ADDA 1.4.0. Retrieved from https://github.com/adda-team/adda/raw/v1.4.0/doc/manual.pdf

Yurkin, M.A., & Hoekstra, A. G. (2007). The discrete dipole approximation: An overview and recent developments. *Journal of Quantitative Spectroscopy and Radiative Transfer*, *106*(1–3), 558–589. https://doi.org/10.1016/j.jqsrt.2007.01.034

Yurkin, Maxim A., & Hoekstra, A. G. (2011). The discrete-dipole-approximation code ADDA: Capabilities and known limitations. *Journal of Quantitative Spectroscopy and Radiative Transfer*, *112*(13), 2234–2247. https://doi.org/10.1016/j.jqsrt.2011.01.031

Zhang, X., Xu, X., Chen, H., Hu, X.-M., & Gao, L. (2022). Dust-planetary boundary layer interactions amplified by entrainment and advections. *Atmospheric Research*, *278*, 106359. https://doi.org/10.1016/j.atmosres.2022.106359